POLITECNICO DI TORINO
Repository ISTITUZIONALE

Electrodeposition in Structural Lattices of Variable Architectures

Original
Electrodeposition in Structural Lattices of Variable Architectures / Kwon, Y., Zhang, J., Musso, G., Rotta Loria, A.F.. - In: ADVANCED ENGINEERING MATERIALS. - ISSN 1527-2648. - (2026), pp. 1-14. [10.1002/adem.71325]

Availability:
This version is available at: 11583/3016716 since: 2026-10-16T09:58:15Z

Publisher:
Wiley

Published
DOI:10.1002/adem.71325

Terms of use:

This article is made available under terms and conditions as specified in the corresponding bibliographic description in the repository

Publisher copyright

(Article begins on next page)

26 November 2026

Check for updates

Advanced Engineering Materials

ADVANCED ENGINEERING MATERIALS
www.aem-journal.com

RESEARCH ARTICLE OPEN ACCESS

Electrodeposition in Structural Lattices of Variable Architectures

Yeong-Man Kwon[1] | Jingwen Zhang[2] | Guido Musso[2] | Alessandro F. Rotta Loria[3]

[1]Department of Civil Engineering, Pukyong National University, Busan, Republic of Korea | [2]Department of Structural, Building and Geotechnical Engineering, Polytechnic University of Turin, Turin, Italy | [3]Subsurface Opportunities + Innovations Laboratory, Department of Civil and Environmental Engineering, Northwestern University, Evanston, Illinois, USA

Correspondence: Alessandro F. Rotta Loria (af-rottaloria@northwestern.edu)

Received: 30 January 2026 | **Revised:** 24 September 2026 | **Accepted:** 25 September 2026

Keywords: architected materials | composite materials | electrodeposition | seawater | structural healing

ABSTRACT

The development of approaches that can autonomously fill and heal material voids and yield composites with tailorable properties is increasingly relevant in engineering. Here, we experimentally and numerically investigate the potential of electrodeposition to engineer stainless-steel lattice scaffolds with variable structures immersed in seawater. Applied voltages of 2–4 V for up to 168 h govern mineral composition, shifting precipitation from Ca-enriched to Mg-dominant. Deposits consist primarily of $CaCO_3$ and $Mg(OH)_2$ polymorphs, with the former accounting for ~21% of the mineral fraction at 2 V and the latter reaching ~92%–94% at 3–4 V. Lattices can gain up to 420 mg of minerals, ~135% of their untreated mass. The mineralization is enhanced at lattice boundaries, corners, and struts by geometry-dependent electric-field localization. Mechanically, electrodeposition reduces stress at 8% strain from 53.4 to 34.0 MPa in the small-opening lattice, which shows a ductile response, while increasing peak stress from 11.7 to 13.5 MPa and residual stress from 4.9 to 10.1 MPa in the large-opening lattice, which shows a brittle response. Altogether, the results of this work show that electrodeposition enables geometry-sensitive, autonomous void filling, modification of chemical and mechanical properties, and the potential to grow architected composites with electricity.

1 | Introduction

Void formation, cracking, and progressive loss of material continuity remain pervasive degradation modes in civil and mechanical infrastructure systems [1, 2]. In reinforced concrete and underground structures, corrosion-driven expansion, chemical attacks, and prolonged environmental exposure often generate excessively large internal voids and fracture networks that undermine structural integrity [3–5]. In metallic joints and composite assemblies, different mechanisms, such as interfacial debonding, fatigue-induced microcracking, and localized material loss, can accumulate over extended service periods, eventually compromising functional continuity [6, 7].

Across these diverse material classes, the ability of a structural system to retain or, when necessary, recover its internal continuity is a critical determinant of long-term durability [8, 9]. When voids proliferate through shrinkage, chemical degradation, cyclic loading, or environmental cycling, the structural performance degrades, maintenance costs escalate, and service life is shortened [10]. In fact, strength is rarely the governing variable for long-term infrastructure durability; pore-size and discontinuity-dependent properties, such as permeability, are the crucial variables of interest [11]. These challenges underscore the growing demand for engineered strategies capable of controllably filling or refilling internal voids to restore continuity and support the resilience, extended lifetime, and sustainability of infrastructure.

This is an open access article under the terms of the Creative Commons Attribution License, which permits use, distribution and reproduction in any medium, provided the original work is properly cited.

© 2026 The Author(s). *Advanced Engineering Materials* published by Wiley-VCH GmbH.

Natural and engineering practices both offer conceptual inspiration. In biological materials such as bone or shells, mineral deposition processes progressively fill porous regions generated by mechanical use, thereby continuously restoring internal cohesion [12]. At the engineering scale, crack repair in reinforced concrete or permeation grouting in soil systems operate based on a similar principle: an existing structural framework (e.g., scaffold) provides stability, whereas a secondary phase (e.g., repair mortar, grout, or bacteria) is introduced to refill voids and restore integrity [13–16]. However, these approaches often suffer from practical limitations: grouted filling tends to be slow, difficult to direct in space and time, and is constrained by environmental and accessibility factors [17, 18].

Recently, electrodeposition has emerged as a promising alternative for autonomous crack healing and void filling [11, 19–25]. The technique eliminates the need for bulky external injections, relying instead on electrical stimulation to precipitate inorganic phases directly within cracks or voids. Studies have demonstrated that electrodeposition can seal cracks in concrete and cement soils by depositing minerals that decrease permeability and mitigate corrosive degradation around steel reinforcements. Because the process is driven by a low-voltage direct current and proceeds autonomously once an electric field is applied, it offers a flexible, repeatable, and potentially scalable path for in situ structural repair with minimal human intervention.

Nevertheless, to the best of our knowledge, no study has explored the coupling between the architecture of engineered materials serving as a host and the process of electrodeposition, which is fundamentally dependent on kinetics and transport phenomena. This gap limits a comprehensive understanding of how the geometry and electrochemical parameters control the deposition uniformity, filling efficiency, and long-term mechanical restoration driven by electrodeposition in porous structures.

In this context, architected metallic scaffolds are attractive host materials because they can provide a well-defined, controllable backbone structure in which void spaces and connectivity can be precisely designed [26]. By coupling such scaffolds with electrodeposition, we propose a simplified yet versatile platform for studying void-filling behavior under controlled and reproducible conditions. In addition to studying the fundamental deposition behavior, we examine the chemical and mechanical properties of the mineralized composites with respect to the electrodeposition process in seawater.

Through controlled electrodeposition experiments and subsequent chemo-mechanical characterizations, we evaluate the effect of internal filling on mineral composition, spatial coverage, stiffness, strength, and overall structural integrity. Our results show that electrodeposition in a designed metallic scaffold can restore continuity and recover, or even improve, mechanical performance. This integrated approach demonstrates the promise of low-voltage, additive-free, flexible electrochemical void filling as a practical route for the in situ repair and reinforcement of porous structures, bridging microscale material processes with macroscale engineering demands.

2 | Results and Discussion

2.1 | Theoretical Background: Electrochemical Reactions During Electrodeposition

Electrodeposition in seawater is driven by coupled electrochemical reactions that occur at the metal–electrolyte interface [27–29]. Upon the application of an electrical stimulation, oxidation reactions at the anode consume water or hydroxide ions (OH^-), producing oxygen gas and releasing electrons, as follows

$$H_2O_2 \rightleftharpoons O_2(\uparrow) + 2H^+ + 2e^- \quad \text{(I)}$$

$$4OH^- \rightleftharpoons O_2(\uparrow) + 2H_2O + 4e^- \quad \text{(II)}$$

$$2H_2O \rightleftharpoons O_2(\uparrow) + 4H^+ + 4e^- \quad \text{(III)}$$

The resultant anode-facing region becomes locally acidic, while ionic concentration gradients develop within the electrolyte. Ionic transport through the void networks surrounding the scaffold occurs through a combination of diffusion driven by these concentration gradients and electromigration driven by the applied electric field.

The electrons released at the anode travel through the external circuit and arrive at the cathode, where reduction reactions occur. Under moderate potentials within the oxygen reduction regime, the dissolved oxygen is reduced to yield OH^- as follows

$$O_2 + 2H_2O + 2e^- \rightleftharpoons H_2O_2 + 2OH^- \quad \text{(IV)}$$

When the applied potential is increased to achieve the water reduction regime, water itself is reduced, generating additional OH^- while evolving hydrogen gas, as follows

$$2H_2O + 2e^- \rightleftharpoons H_2(\uparrow) + 2OH^- \quad \text{(V)}$$

This local OH^- production increases the interfacial pH, which shifts the carbonate/bicarbonate equilibria in seawater and triggers the precipitation of solid mineral phases: magnesium hydroxide ($Mg(OH)_2$) forms preferentially under strongly alkaline conditions, while calcium carbonate ($CaCO_3$) precipitates when carbonate ions (CO_3^{2-}) become sufficiently concentrated and pH conditions permit [19, 30, 31] as follows

$$Mg^{2+} + 2OH^- \rightarrow Mg(OH)_2(\downarrow) \quad \text{(VI)}$$

$$CO_2 + H_2O \rightleftharpoons H_2CO_3 \rightleftharpoons H^+ + HCO_3^- \rightleftharpoons H^+ + CO_3^{2-} \quad \text{(VII)}$$

$$OH^- + HCO_3^- \rightleftharpoons H_2O + CO_3^{2-} \quad \text{(VIII)}$$

$$Ca^{2+} + CO_3^{2-} \rightarrow CaCO_3(\downarrow) \quad \text{(IX)}$$

$$Ca^{2+} + HCO_3^- + OH^- \rightarrow H_2O + CaCO_3(\downarrow) \quad \text{(X)}$$

The precipitation of these minerals is the fundamental mechanism driving the formation of composite materials starting from cathodic scaffolds of engineered architectures. While these composite materials form, the H^+ and OH^- ions produced at the electrodes diffuse over time into the electrolyte and neutralize through ionic recombination

15272648, 0, Downloaded from https://advanced.onlinelibrary.wiley.com/doi/10.1002/adem.71325 by Guido Musso - Politecnico Di Torino Sist. Bibl Del Polit Di Torino , Wiley Online Library on [14/10/2026]. See the Terms and Conditions (https://onlinelibrary.wiley.com/terms-and-conditions) on Wiley Online Library for rules of use; OA articles are governed by the applicable Creative Commons License

$$H^+ + OH^- \rightleftharpoons H_2O \quad \text{(XI)}$$

2.2 | Time-Dependent Electrodeposition Within Lattice Scaffolds

Figure 1 illustrates the temporal evolution of mineral deposition within the 3D-printed lattice scaffolds subjected to constant-voltage (3 V) electrodeposition in ASTM D1141-98 artificial seawater [32]. The two scaffolds are referred to as the small-opening lattice and large-opening lattice, corresponding to clear square opening widths of 0.5 and 1.0 mm, respectively; Table 1 provides detailed geometric descriptors. The 0-V immersion-only control showed negligible mass change and no substantial mineral infilling after 168 h for both lattice geometries, indicating that passive immersion effects were limited under the conditions used here (Figure S1). To better define the electrochemical conditions at the lattice–seawater interface, the measured current was normalized by the scaffold surface area, A_s, and reported as current density, J, for all applied voltages (Figure S2). The current–density traces generally decreased with time, consistent with progressive deposit accumulation and increasing electrochemical or transport resistance within the lattice. The cumulative charge, Q, obtained by integrating the measured current further showed that the electrical exposure was not simply proportional to the applied voltage (Figure S3A,B). Although 4 V produced the highest initial current and the fastest initial charge accumulation, its rapid current decay caused the Q at 3 V to exceed that at 4 V within the first several hours and remain higher over longer treatment periods for both lattice geometries. Probe-based pH measurements further showed the development of alkaline near-cathode conditions during electrodeposition (Figure S4). Under these electrochemical and pH conditions, the precipitation of $Mg(OH)_2$ (i.e., brucite) and $CaCO_3$ polymorphs within and around the scaffold framework (Figure 1A) was reflected in the time-dependent morphological evolution of the deposits (Figure 1B,C). The 168-h condition is therefore interpreted as a trade-off between deposition rate, interior penetration, and deposit stability rather than an attempt to maximize short-term mineral mass.

In the small-opening lattice geometry (Figure 1B), electrodeposition was initiated with thin mineral layers formed along the beam surfaces at 1 h, followed by progressive narrowing and apparent filling of the internal void regions between 8 and 24 h. During this period, optical images showed that the deposits thickened along the lattice beams and progressively extended into the adjacent openings. At 72–168 h, the scaffold interior appeared visually

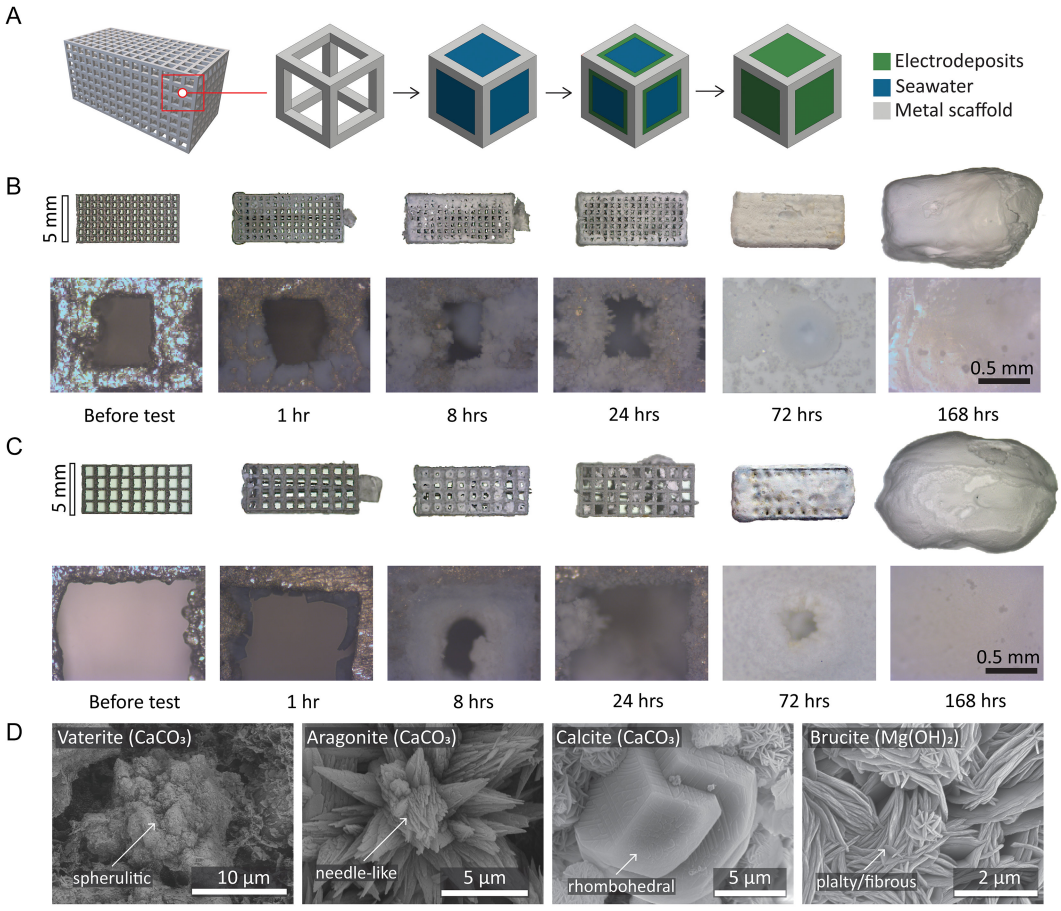


FIGURE 1 | Time-dependent electrodeposition behavior within lattice scaffolds. (A) Schematic illustrating the progressive infilling of a lattice unit during electrodeposition. Colors indicate the metal scaffold (gray), seawater (blue), and deposited minerals (green). (B) Time-lapse images of the small-opening lattice, including macroscopic (top) and optical (bottom) views from 1 to 168 h. (C) Corresponding images for the large-opening lattice over the same time intervals. (D) Representative SEM micrographs showing the principal mineral phases: vaterite, aragonite, and calcite ($CaCO_3$ polymorphs), and brucite ($Mg(OH)_2$).

15272648, 0, Downloaded from https://advanced.onlinelibrary.wiley.com/doi/10.1002/adem.71325 by Guido Mosso - Politecnico Di Torino Sist. Bibl Del Polit Di Torino , Wiley Online Library on [14/10/2026]. See the Terms and Conditions (https://onlinelibrary.wiley.com/terms-and-conditions) on Wiley Online Library for rules of use; OA articles are governed by the applicable Creative Commons License

TABLE 1 | Geometric descriptors of the 3D-printed 316L stainless-steel lattice scaffolds used in this study.

Scaffold geometry	Small-opening lattice	Large-opening lattice
Nominal beam thickness, *B,* mm	0.2	0.2
Clear opening width, *H,* mm	0.5	1.0
Unit-cell size, $a = B + H$, mm	0.7	1.2
Effective strut span, *L,* mm	0.5	1.0
Slenderness, L/B, —	2.5	5.0
Outer dimensions, width × depth × height, mm^3	5.1 × 5.1 × 10.7	5.0 × 5.0 × 11
Surface area, A_s, mm^2	1126.4	510
Porosity, *n*, %	77.28	90.18

filled at the optical microscopy scale, forming a consolidated mineral network of uniform thickness. The confined geometry of the small-opening lattice appeared to promote rapid pore filling as the ion-transport pathways became narrow and supersaturation was locally enhanced [33, 34].

A similar temporal trend was observed in the large-opening lattice (Figure 1C), although with slower interior accumulation at early times. The larger void volume likely delayed the build-up of locally favorable precipitation conditions, resulting in less uniform deposition during the first 24 h. Nevertheless, by 72–168 h, substantial mineral growth occurred throughout the scaffold, indicating that both geometries ultimately supported mineral penetration into the scaffold interior.

Scanning electron microscopy (SEM) observations and X-ray diffraction (XRD) analysis revealed that the deposits predominantly consisted of brucite and $CaCO_3$ polymorphs (Figures 1D and S5). Brucite manifested as fibrous or platy aggregates, whereas $CaCO_3$ appeared as vaterite spherulites, aragonite needles, and rhombohedral calcite. The coexistence of these phases reflects the coupled chemical pathways active during electrodeposition; the alkaline near-cathode conditions observed during electrodeposition (Figure S4) favor brucite nucleation, whereas the simultaneous shift in carbonate equilibrium subsequently supports the formation of multiple calcium carbonate polymorphs [35]. Together, time-lapse observations, microscopy, and XRD analysis demonstrate that electrodeposition in seawater produces progressive mineral infilling within metallic lattices, with growth kinetics and internal coverage dependent on the scaffold geometry.

2.3 | Influence of Applied Voltage on Mineral Growth and Composition

Figure 2 illustrates how the applied voltage governed both the rate and chemistry of the electrodeposited minerals within the small-opening lattice scaffold. At 2 V, mineral deposition progressed slowly, with thin surface layers forming after 24 h and moderate interior accumulation appearing only after 72–168 h (Figure 2A). The relatively low *J* (Figure S2A) and weaker near-cathode alkalinization under this condition (Figure S4A) are consistent with a lower cathodic driving force for mineral precipitation. As a result, the interior of the scaffold remained partially open even at extended times, indicating that low-voltage operation favored gradual pore filling and coating development.

At 3 V, both the rate of mineral growth and the degree of interior occlusion increased. The higher *J* (Figure S2B) and stronger near-cathode alkalinization at 3 V (Figure S4B) suggested an enhanced cathodic driving force for brucite and $CaCO_3$ precipitation, likely with a greater contribution from water reduction [23, 36]. The mineral deposits thickened more rapidly along the beam surfaces and propagated inward between 24 and 72 h, ultimately producing a visually dense mineral framework after 168 h.

By contrast, at 4 V, the highest initial *J* (Figure S2C) and strongest near-cathode alkalinization (Figure S4C) were observed, and mineral growth became rapid and spatially nonuniform. The interior regions appeared rapidly infilled, whereas the exterior surfaces developed encapsulating shells as early as 72 h (Figure 2A). The higher applied voltage likely promoted hydrogen evolution, generating gas bubbles that can block active deposition sites, disrupt mineral consolidation, reduce contact continuity between the mineral phase and scaffold, and facilitate shell detachment [22, 36–38]. These effects likely contributed to the nonuniform exterior shell formation and partial detachment observed at 4 V.

Quantitative measurements of net mineral mass (M_m) further highlighted the voltage dependence of mineral accumulation (Figure 2B). M_m generally increased from 2 to 3 V, which is consistent with enhanced cathodic reactions and accelerated mineral precipitation. At 4 V, however, M_m plateaued or decreased under some conditions, consistent with the unstable exterior shell formation and partial detachment observed at high voltage. Charge normalization, M_m/Q, provided a complementary assessment of the voltage dependence of mineral accumulation (Figure S3C,D). For the small-opening lattice, M_m/Q increased with applied voltage at the treatment times of 24, 72, and 168 h. Thus, the lower retained M_m at 4 V than at 3 V was not associated with a lower M_m/Q but occurred together with a lower *Q* and the unstable shell growth and partial detachment observed at 4 V.

The applied voltage also influenced the chemical composition and crystalline phase assemblage of the electrodeposited minerals, as shown by the SEM images with energy-dispersive X-ray spectroscopy (EDS) mapping (Figure 2C) and XRD

15272648, 0, Downloaded from https://advanced.onlinelibrary.wiley.com/doi/10.1002/adem.71325 by Guido Musso - Politecnico Di Torino Sist. Bibl Del Polit Di Torino , Wiley Online Library on [14/10/2026]. See the Terms and Conditions (https://onlinelibrary.wiley.com/terms-and-conditions) on Wiley Online Library for rules of use; OA articles are governed by the applicable Creative Commons License

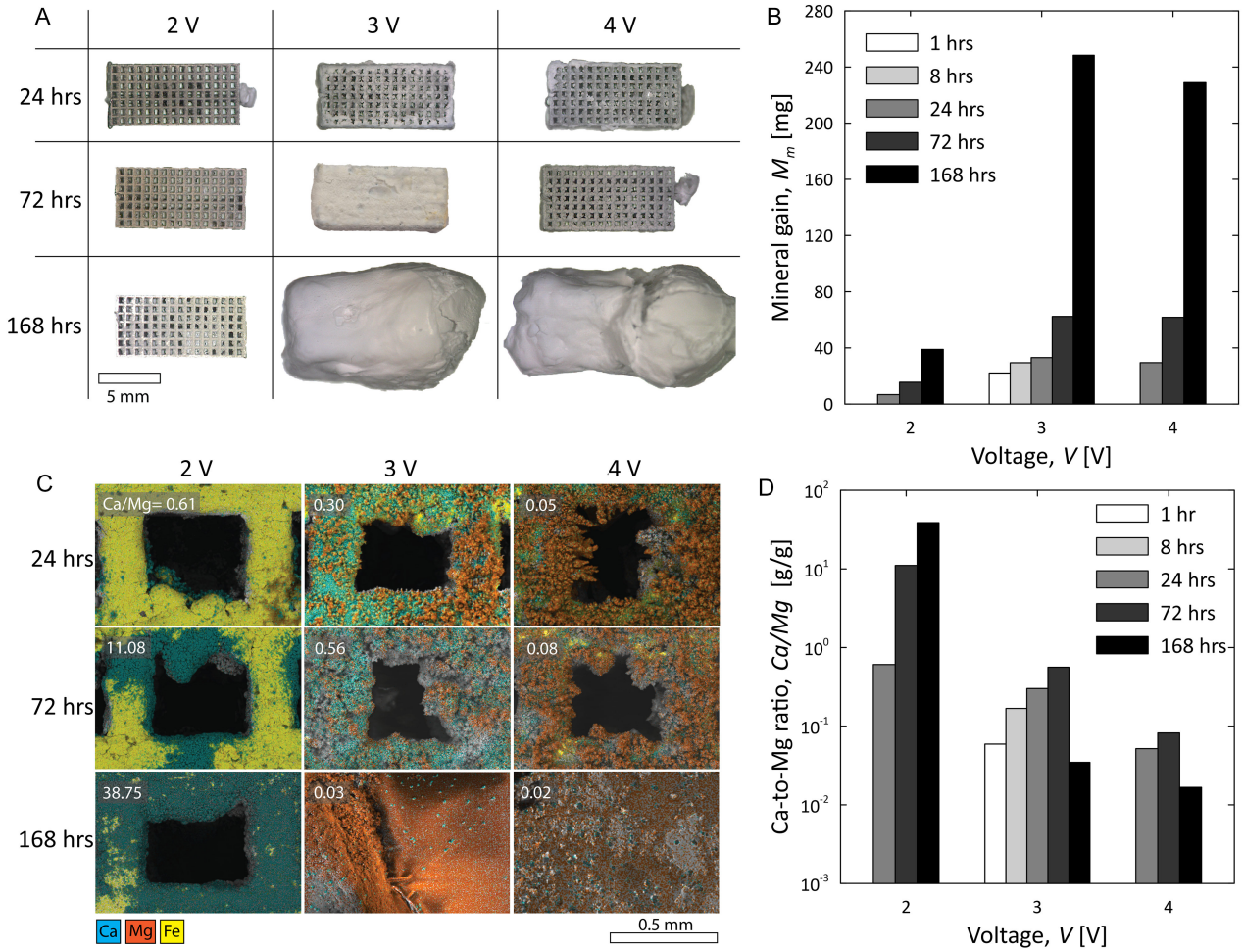


FIGURE 2 | Voltage-dependent mineral deposition and compositional evolution on lattice scaffolds. (A) Electrodeposits formed on the small-opening lattice at 2, 3, and 4 V after 24, 72, and 168 h, illustrating interior mineral accumulation and exterior encapsulation at longer durations. (B) Mineral gain, M_m, representing the net deposited mineral mass for each condition. (C) SEM–EDS composite images showing Ca, Mg, and Fe distributions at the same time points, with reported Ca/Mg values corresponding to area-averaged mass ratios. (D) Ca-to-Mg mass ratios, Ca/Mg, plotted on a logarithmic scale, emphasizing voltage-induced compositional shifts.

analysis (Figure S5). At 2 V, the deposits retained a relatively larger Ca-bearing contribution, as reflected by higher Ca/Mg ratios and a larger fraction of crystalline $CaCO_3$ polymorphs. As the applied voltage increased to 3 and 4 V, the deposits shifted toward Mg-rich, brucite-dominant assemblages. This trend was consistent with the voltage-dependent near-cathode alkalinization (Figure S4), which favors $Mg(OH)_2$ precipitation while modifying carbonate speciation and the relative formation of $CaCO_3$ polymorphs. The logarithmic plot of the Ca/Mg ratios (Figure 2D) captures these compositional transitions, indicating that the applied voltage shifted the mineralization regime from Ca-enriched to Mg-rich precipitation. Overall, these results demonstrate that the applied voltage not only controls mineral accumulation but also tunes the resulting mineral chemistry within the metal lattice scaffolds.

2.4 | Effects of Scaffold Geometry on Electrodeposition Efficiency and Mineral Composition

Figure 3 compares the electrodeposition behavior of lattice scaffolds with different opening sizes, highlighting the role of scaffold geometry in controlling mineral distribution, accumulation, and composition under identical electrochemical conditions. Although both geometries underwent substantial mineralization after prolonged stimulation, the small- and large-opening lattices exhibited distinct deposition patterns because differences in void size and porosity modified ion accessibility, available deposition volume, and the evolution of local precipitation conditions.

After 7 days of electrodeposition (Figure 3A), the small-opening lattice exhibited visually dense interior occlusion with relatively limited exterior shell formation, indicating that mineral growth was more concentrated within the confined internal void space. This behavior is consistent with restricted transport pathways that may promote local ion accumulation and supersaturation within the lattice openings. By contrast, the large-opening lattice displayed a thicker exterior mineral envelope at all voltages, particularly at 4 V, when the outer shell became sufficiently thick to detach from the scaffold surface. Despite this partial spalling, the interior of the large-opening lattice remained well-filled, demonstrating that open geometries still supported mineral penetration into the scaffold interior while promoting greater deposition along the exterior boundary.

15272648, 0, Downloaded from https://advanced.onlinelibrary.wiley.com/doi/10.1002/adem.71325 by Guido Mosso - Politecnico Di Torino Sist. Bibl Del Polit Di Torino , Wiley Online Library on [14/10/2026]. See the Terms and Conditions (https://onlinelibrary.wiley.com/terms-and-conditions) on Wiley Online Library for rules of use; OA articles are governed by the applicable Creative Commons License

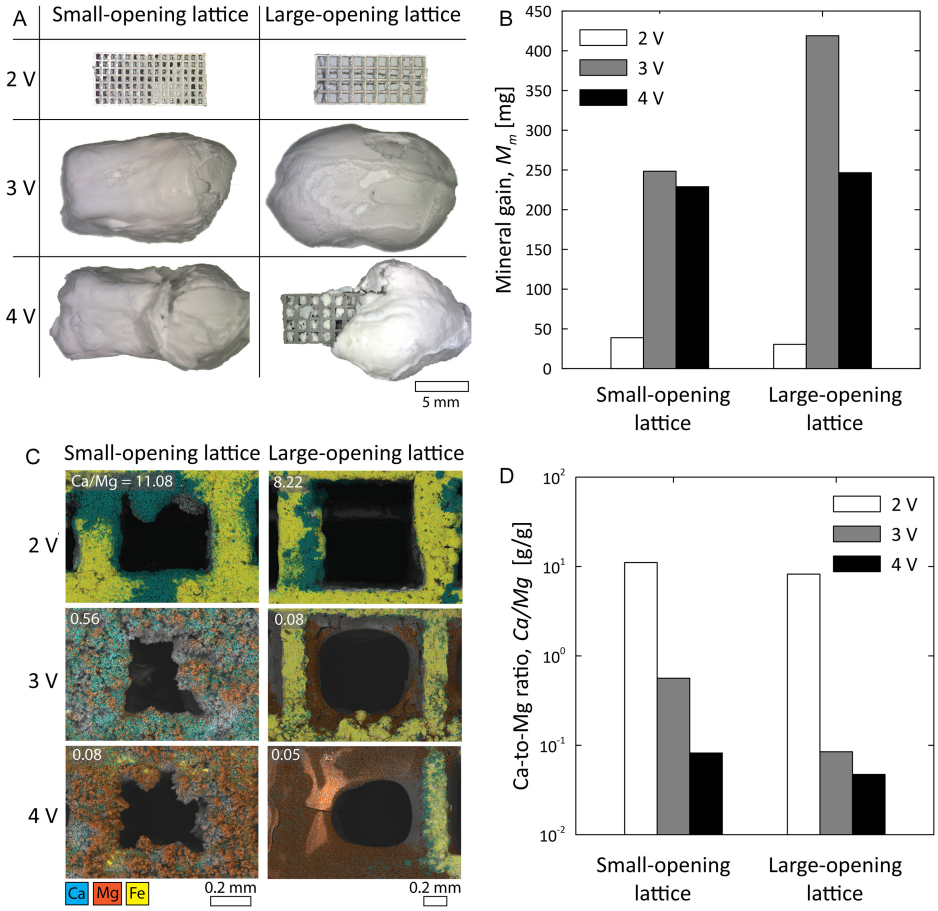


FIGURE 3 | Effects of scaffold geometry on mineral accumulation and composition under different voltage conditions. (A) Electrodeposits formed on the two lattice geometries after 7 days at 2, 3, and 4 V. (B) Mineral gain, M_m, comparing the two geometries under each voltage. (C) SEM–EDS composite images of deposits formed after 3 days, showing distinct Ca, Mg, and Fe spatial distributions and geometry-dependent Ca/Mg differences between the geometries. (D) Ca-to-Mg mass ratios, Ca/Mg, on a logarithmic scale, highlighting geometry-dependent compositional variations.

Quantitative measurements of the mineral mass (M_m) showed that the influence of scaffold geometry depended on the applied voltage (Figure 3B). The M_m values of the two lattices were relatively similar at 2 and 4 V, whereas the large-opening lattice accumulated more minerals than the small-opening lattice at 3 V. This pronounced difference at 3 V is consistent with the greater ion accessibility and available deposition volume associated with the higher porosity and larger opening width of the large-opening lattice. Charge-normalized analysis further showed that the large-opening lattice exhibited a higher M_m/Q at 3 V (Figure S3D), indicating that its greater M_m under this condition cannot be attributed solely to the higher Q. These results suggest that the influence of scaffold geometry on mineral accumulation depends on the applied electrochemical conditions.

Geometry also influenced mineral composition in a voltage-dependent manner. The geometry-dependent compositional difference was most pronounced at 3 V, where the area-averaged Ca/Mg ratios differed by more than one order of magnitude (Figure 3C,D), whereas the differences between the two geometries were considerably smaller at 2 and 4 V. These variations likely reflect coupled differences in J and Q evolution (Figures S2 and S3), ion transport, and near-electrode pH development (Figure S4). In the small-opening lattice, early apparent filling of the confined voids may have increased transport resistance and restricted continued ion exchange. By contrast, the higher porosity and larger openings of the large-opening lattice maintained more accessible transport pathways, favoring Mg-rich precipitation conditions.

2.5 | Numerical Analysis of Geometry-Dependent Electric-Field Distributions

Figure 4 presents the simulated electric field distributions within different geometries. Under an applied potential difference of 3 V, the surface and internal cross-sectional maps (Figure 4A,B) revealed heterogeneous field distributions. The electric field was concentrated primarily along the outer boundaries, corners, and struts of the lattice cathodes, where geometric discontinuities occurred. In contrast, the open lattice voids and interior regions exhibited substantially lower magnitudes but a more homogeneous distribution. The 3D results (Figure 4C) further showed that the electric field magnitude increased with increasing potential difference while the

15272648, 0, Downloaded from https://advanced.onlinelibrary.wiley.com/doi/10.1002/adem.71325 by Guido Mosso - Politecnico Di Torino Sist. Bibl Del Polit Di Torino , Wiley Online Library on [14/10/2026]. See the Terms and Conditions (https://onlinelibrary.wiley.com/terms-and-conditions) on Wiley Online Library for rules of use; OA articles are governed by the applicable Creative Commons License

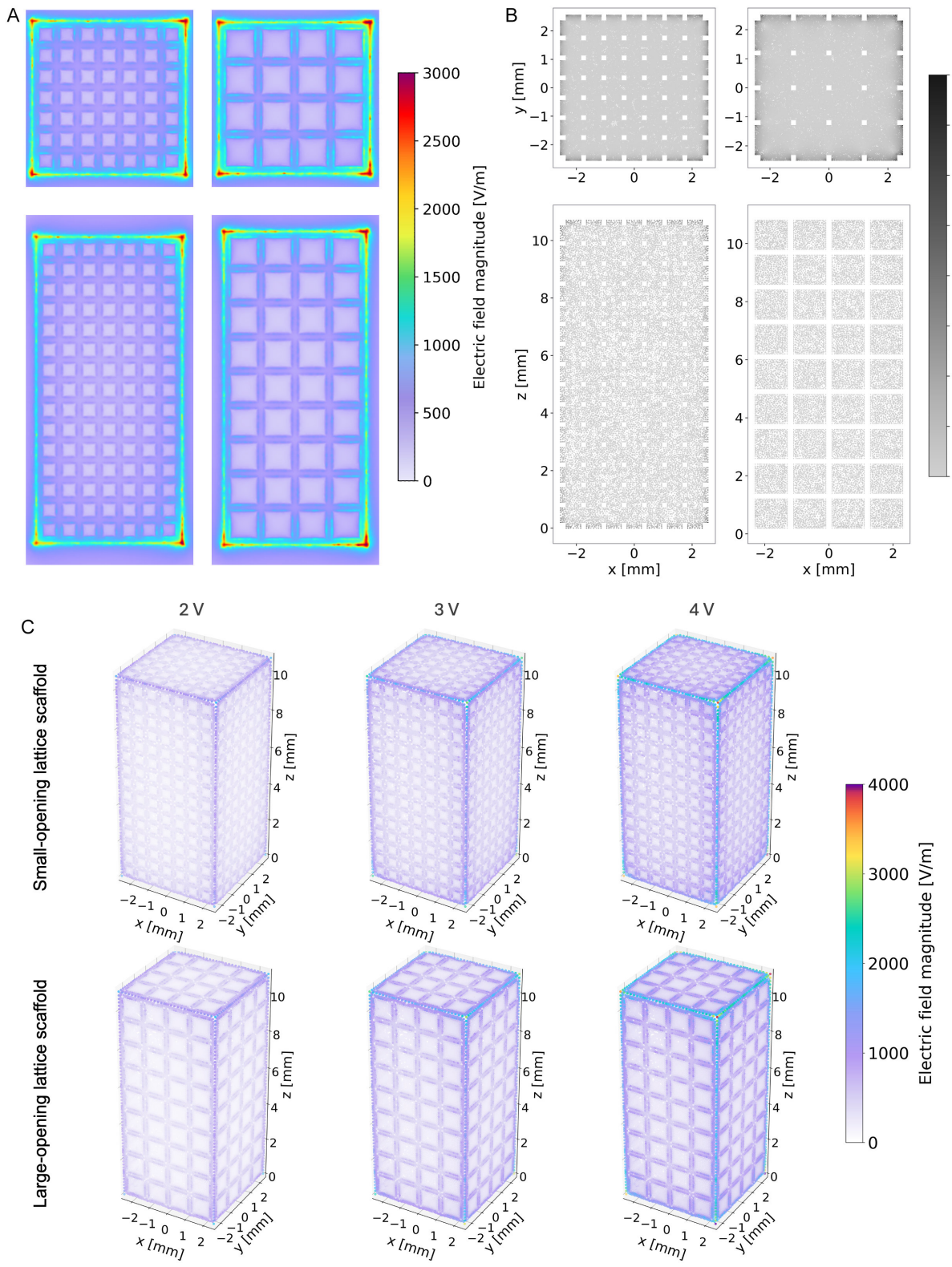


FIGURE 4 | Simulated electric-field distributions within the small-opening and large-opening lattice scaffolds. (A) Electric field distributions at an applied potential difference of 3 V on the top surfaces (first row) and side surfaces (second row) of the small-opening scaffold (left) and large-opening scaffold (right). (B) Electric field distributions at 3 V on horizontal center-plane sections (first row) and vertical center-plane sections (second row) of the small-opening scaffold (left) and large-opening scaffold (right). (C) 3D electric field distributions throughout the small-opening scaffold (top row) and large-opening scaffold (bottom row) under applied potential differences of 2, 3, and 4 V.

spatial locations of the principal field-enhancement regions remained consistent. These predicted high-field regions qualitatively corresponded to locations where early-stage mineral deposition was observed experimentally, suggesting that localized electric-field enhancement may contribute to preferential mineral nucleation.

15272648, 0, Downloaded from https://advanced.onlinelibrary.wiley.com/doi/10.1002/adem.71325 by Guido Mosso - Politecnico Di Torino Sist. Bibl Del Polit Di Torino , Wiley Online Library on [14/10/2026]. See the Terms and Conditions (https://onlinelibrary.wiley.com/terms-and-conditions) on Wiley Online Library for rules of use; OA articles are governed by the applicable Creative Commons License

2.6 | Effect of Mineral Growth on the Lattice Strength

The compressive responses of the lattice scaffolds (Figure 5) revealed that the strength evolution upon electrodeposition was governed primarily by geometry-dependent load-bearing mechanisms rather than by the intrinsic strength of the deposited minerals. The apparent compressive modulus, E_{app}, evaluated at a reference strain of 1%, and characteristic stress metrics were therefore extracted from the compression curves: $\sigma_{8\%}$ for the peak-free response of the small-opening lattice and σ_{peak} and σ_{res} for the buckling-dominated response of the large-opening lattice (Table S1). Replicate-level distributions of these metrics are summarized in Figure S6.

In the untreated reference state, the two lattice geometries displayed different deformation behaviors. The small-opening lattice, with its lower porosity and shorter effective strut span, showed a ductile response with a high E_{app} (Figure 5A) [39]. The curve consists of two quasi-linear regimes: an initial steep slope associated primarily with axial strut loading, followed by a less steep regime associated with progressive strut bending, node rotation, and interstrut contact. This transition reflected gradual densification without localized instability or abrupt load shedding. In contrast, the large-opening lattice showed a brittle response with a pronounced σ_{peak} followed by stress reduction and a residual plateau, σ_{res} (Figure 5B), indicating buckling-dominated deformation of slender struts and subsequent load redistribution [40]. Electrodeposition affected these two architectures in distinct ways by interacting with their respective deformation mechanisms. For the small-opening lattice (Figure 5A), mineral deposition reduced both E_{app} and $\sigma_{8\%}$ (Figure S6A,B), indicating that the mineral infill acted primarily as a compliant phase within the lower-porosity lattice architecture [41, 42]. The overall deformation mode remained unchanged, with the response still being governed by progressive densification rather than localized buckling. By contrast, the large-opening lattice (Figure 5B) showed increased σ_{peak} and σ_{res} after electrodeposition (Figure S6C,D), consistent with mineral growth providing additional support to slender struts, delaying buckling, and enhancing postbuckling load redistribution.

Across both lattice designs, electrodeposition reduced E_{app}, reflecting the incorporation of a mechanically softer mineral infill into the stainless-steel lattice. During compression, local microcracking or crushing of the mineral infill may have contributed to stress redistribution and a more gradual deformation response. Although interfacial adhesion is important for mineralized composite systems, the compression tests performed here characterize the apparent structural response of the lattices rather than the intrinsic scaffold–mineral bond strength. Dedicated adhesion tests will be required in future work to quantitatively assess this interface.

3 | Concluding Remarks

This study demonstrated that electrodeposition can serve as an effective and controllable mechanism for filling internal voids within structured metallic lattices while simultaneously tuning their chemical and mechanical properties. By combining 3D-printed stainless-steel scaffolds with electrically driven mineral precipitation in artificial seawater, we established a simplified experimental platform to isolate the coupling between scaffold geometry, electrochemical transport, and mineral growth behavior.

Systematic experiments revealed that the applied voltage governs both the kinetics and chemistry of mineral deposition. Moderate voltages promoted balanced Ca- and Mg-based precipitation with progressive interior filling, whereas higher voltages accelerated brucite-dominated growth, accompanied by H_2 evolution and deposition instability.

Scaffold geometry further modulates the spatial distribution and amount of mineral growth. The small-opening lattice promoted

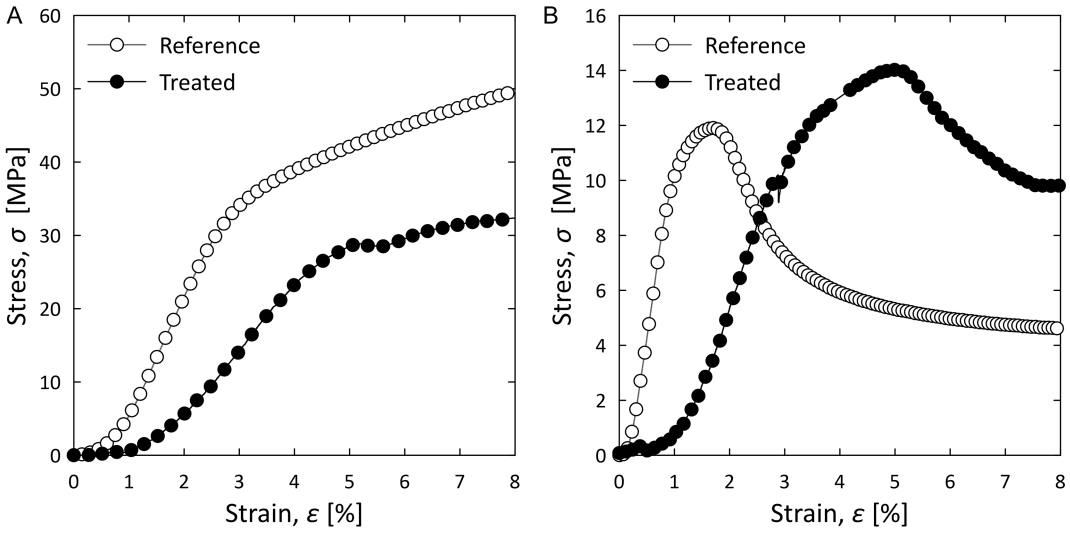


FIGURE 5 | Compressive stress–strain behavior of 3 V, 7-day mineralized lattice scaffolds and untreated scaffolds. (A) Small-opening lattice and (B) large-opening lattice. In the small-opening lattice, electrodeposition reduced the apparent compressive modulus, E_{app}, and stress level, σ, over the tested strain range, whereas in the large-opening lattice, electrodeposition increased the peak, σ_{peak}, and postbuckling residual stress, σ_{res}.

15272648, 0, Downloaded from https://advanced.onlinelibrary.wiley.com/doi/10.1002/adem.71325 by Guido Musso - Politecnico Di Torino Sist. Bibl Del Polit Di Torino , Wiley Online Library on [14/10/2026]. See the Terms and Conditions (https://onlinelibrary.wiley.com/terms-and-conditions) on Wiley Online Library for rules of use; OA articles are governed by the applicable Creative Commons License

more visually complete internal filling, whereas geometry-dependent differences in mineral accumulation and composition were most pronounced at 3 V, where the large-opening lattice exhibited greater mineral uptake and a stronger Mg-rich compositional shift. Numerical simulations further showed that scaffold geometry produces spatially heterogeneous electric field distributions, with local field enhancement along lattice boundaries, corners, and struts that qualitatively corresponded to preferential sites of early-stage mineral deposition. These results suggest that geometry-dependent electrical driving conditions, together with ion transport and near-electrode chemistry, shape the spatial evolution of mineral growth.

Mechanical testing showed that electrodeposition interacts with geometry-controlled deformation mechanisms. In the small-opening lattice, mineral infill reduced the apparent stiffness and characteristic stress while preserving the progressive densification mode. In contrast, in the large-opening lattice, mineral growth stabilized slender struts, delayed buckling, and enhanced both peak and residual stress. These contrasting responses show that electrodeposition does not impose a uniform strengthening effect; instead, it modifies structural performance according to the underlying lattice architecture.

Collectively, these findings suggest that electrodeposition is a low-energy, additive-free, and geometry-sensitive strategy for autonomous void filling and mechanical modulation of metallic structures. Beyond its immediate relevance to structural repair and crack healing, where treatment times ranging from days to weeks are acceptable for practical applications, as in other civil engineering applications at large, the scaffold-based platform introduced here provides a broadly applicable framework for studying electrochemically guided material growth in complex porous architectures. Future work should quantify scaffold–mineral interfacial adhesion, evaluate transport-controlled filling in larger or more tortuous geometries, and optimize deposition protocols to improve treatment efficiency while maintaining uniform and stable mineral infilling.

4 | Experimental Section

4.1 | Experimental Setup

Figure 6 presents the experimental configuration used to investigate electrically induced mineral growth in 3D-printed lattices. The electrode arrangement (Figure 6A,B) was designed to provide consistent electrochemical exposure across the entire lattice scaffold. The anode was positioned 10 mm above the bottom of the beaker, whereas the cathode was immersed at mid-height to a depth of 60 mm. The electrodes were positioned 60 mm apart and connected to a DC power supply (2280S-32–6; Keithley Instruments, Cleveland, OH). The cathodic scaffold was connected using a 316L stainless-steel wire (diameter = 0.127 mm, Master Wire Supply, Beavercreek, OH, USA), which was threaded through predefined openings around the central strut and routed along the bottom lattice openings to form a mechanically secured loop. The same contact path was used for all specimens, and the submerged cathode wire was Teflon-insulated except for the exposed contact region with the scaffold.

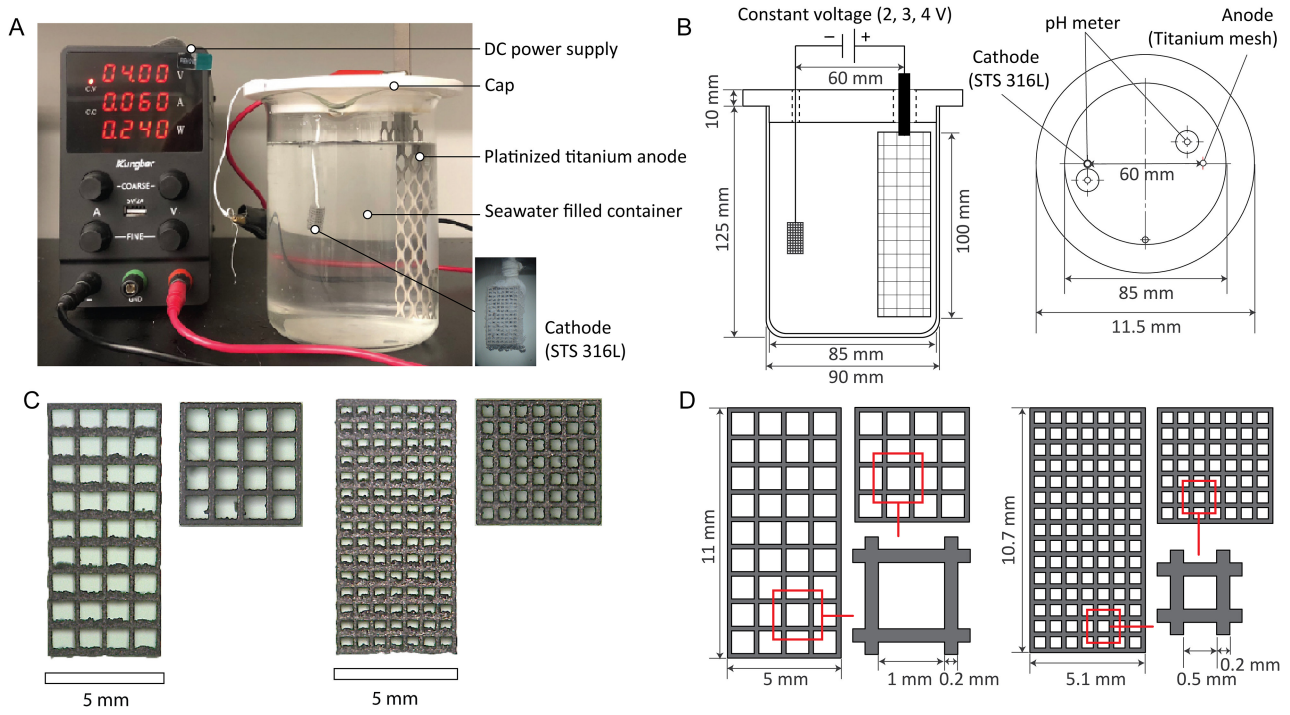


FIGURE 6 | Experimental setup and lattice scaffold geometries for electrodeposition in seawater. (A) Electrodeposition setup consisting of a 3D-printed 316L stainless-steel lattice cathode and a platinized titanium mesh anode fully immersed in seawater and operated under constant-voltage direct current (DC) conditions. (B) Engineering schematics detailing the electrode configuration and container geometry. (C) Pre-electrodeposition large-opening and small-opening lattice scaffolds, shown in side and top views. (D) Engineering drawings highlighting a representative lattice unit defining the two geometries.

15272648, 0, Downloaded from https://advanced.onlinelibrary.wiley.com/doi/10.1002/adem.71325 by Guido Musso - Politecnico Di Torino Sist. Bibl Del Polit Di Torino , Wiley Online Library on [14/10/2026]. See the Terms and Conditions (https://onlinelibrary.wiley.com/terms-and-conditions) on Wiley Online Library for rules of use; OA articles are governed by the applicable Creative Commons License

Previous scaffold design studies in tissue engineering have demonstrated that pore size and void fraction critically influence material filling efficiency, nutrient diffusion, and structural occupancy within porous networks [6]. These findings underscore the importance of scaffold openness when designing 3D structures intended to be infiltrated or filled, a principle that applies to mineral deposition in metallic lattices. Accordingly, we selected two lattice geometries (small- and large-opening lattices; Figure 6C,D) to investigate how scaffold openness and volumetric void fraction affect ion transport, mineral accumulation, and filling behavior. Both geometries were designed with the same nominal beam thickness, $B = 0.2$ mm, but different clear square opening widths, $H = 0.5$ and 1.0 mm. The corresponding geometric descriptors are summarized in Table 1.

4.2 | Fabrication of 3D-Printed Cathodic Scaffolds and Anode

Cathodic scaffolds were produced from 316L stainless-steel powder by direct metal laser sintering through Protolabs (Maple Plain, MN, USA), as 316L stainless-steel offers high corrosion resistance in chloride-rich environments and supports electrochemical stability [43, 44]. CAD models of the lattice geometries were prepared using AutoCAD (Autodesk, San Francisco, CA, USA), converted into sliced images, and printed layer-by-layer by selectively melting the metal powder with a laser. After printing, the parts underwent manufacturer-provided postprocessing, including powder removal and thermal treatment. The finished scaffolds were rinsed with ethanol and air-dried before use. A platinized titanium mesh (5 cm × 10 cm; MXGNSS, Beijing, China) was used as the anode.

4.3 | Electrolyte

Artificial seawater was used as electrolyte and prepared according to ASTM D1141-98 [32] using commercial sea salt (Lake Products Company LLC, Florissant, MO, USA). A total of 41.953 g of sea salt was dissolved in Type I ultrapure water (18.2 MΩ·cm of resistivity at 25 °C; Millipore Sigma, Burlington, MA, USA) and mixed using an electric overhead mixer (ONiLAB OS20-S, San Francisco, CA, USA) until fully dissolved. No electrolyte replenishment was performed during the experiments. Solution pH was measured using pH probes (HI10530, Hanna Instruments, Woonsocket, RI, USA) positioned approximately 0.5 mm from the cathodic scaffold and anode during electrodeposition. The electrolyte temperature remained within 20–22 °C during the experiments.

4.4 | Power Source

Constant voltages of 2, 3, and 4 V were applied for 1, 8, 24, 72, and 168 h using a direct current (DC) power supply. The current evolution during electrodeposition was recorded at each applied voltage. The measured current, I, was normalized by the scaffold surface area, A_s, to obtain the current density, $J = I/A_s$. The cumulative charge passed, Q, was calculated by integrating the measured current over time, $Q(t) = \int_0^t I(\tau)d\tau$, using trapezoidal numerical integration. All experiments were performed under static conditions, and sample evaporation was minimized using a top cover. After electrodeposition, the samples were removed, rinsed with deionized water at least three times to eliminate residual ions, and air-dried at room temperature for at least 48 h. Both m_{before} and m_{after} were measured on air-dried specimens using a precision balance with a readability of 10 mg (Sartorius, Göttingen, Germany).

4.5 | Numerical Simulations

Numerical simulations were conducted to characterize the spatial distribution of electric potential within the electrochemical cell, with particular emphasis on the electric field surrounding and within the cathodic lattice-scaffold. The model was developed in COMSOL Multiphysics 6.4 using the Electric Currents (ec) interface. The numerical model was designed to evaluate the electrical behavior of the electrochemical cell independently of electrochemical reactions and chemical species transport; therefore, changes in ionic concentrations, chemical reactions, and mineral precipitation were not considered. Under the assumption of steady state electrical conduction, charge conservation was imposed throughout the computational domain as

$$\nabla \cdot J = 0 \tag{1}$$

where J is the current density (A/m^2). The current density was related to the electric field through Ohm's law

$$J = \kappa E \tag{2}$$

where κ denotes the electrical conductivity of the material (S/m), and E is the electric field (V/m) defined as $E = -\nabla V$ where V is the electric potential (V).

Combining Equations (1) and (2) gives

$$\nabla \cdot (\kappa E) = 0 \tag{3}$$

Equation (3) was solved throughout the modeled domains to obtain the electric field and current density for the applied potentials.

4.6 | Geometry and Mesh

The model reproduced the configuration of the electrochemical cell used in the experiments and included only the electrolyte-occupied region of the cell. The relative positions and dimensions of the electrodes were maintained according to the experimental setup to ensure consistency between the simulation and experiments (Figure 7). Based on the experimental configurations, small-opening and large-opening lattice scaffolds were considered (Figure 7A,B). The anode was represented by a diamond-mesh plane, with only the portion submerged in the electrolyte included in the model (Figure 7C).

To accurately characterize the electric field within and around each lattice scaffold, local mesh refinement was applied to the electrolyte volume enclosed by the scaffold. A maximum element size of 0.1 mm was specified for this region, while a relatively coarser mesh was used in the remaining electrolyte domain

15272648, 0, Downloaded from https://advanced.onlinelibrary.wiley.com/doi/10.1002/adem.71325 by Guido Musso - Politecnico Di Torino Sist. Bibl Del Polit Di Torino , Wiley Online Library on [14/10/2026]. See the Terms and Conditions (https://onlinelibrary.wiley.com/terms-and-conditions) on Wiley Online Library for rules of use; OA articles are governed by the applicable Creative Commons License

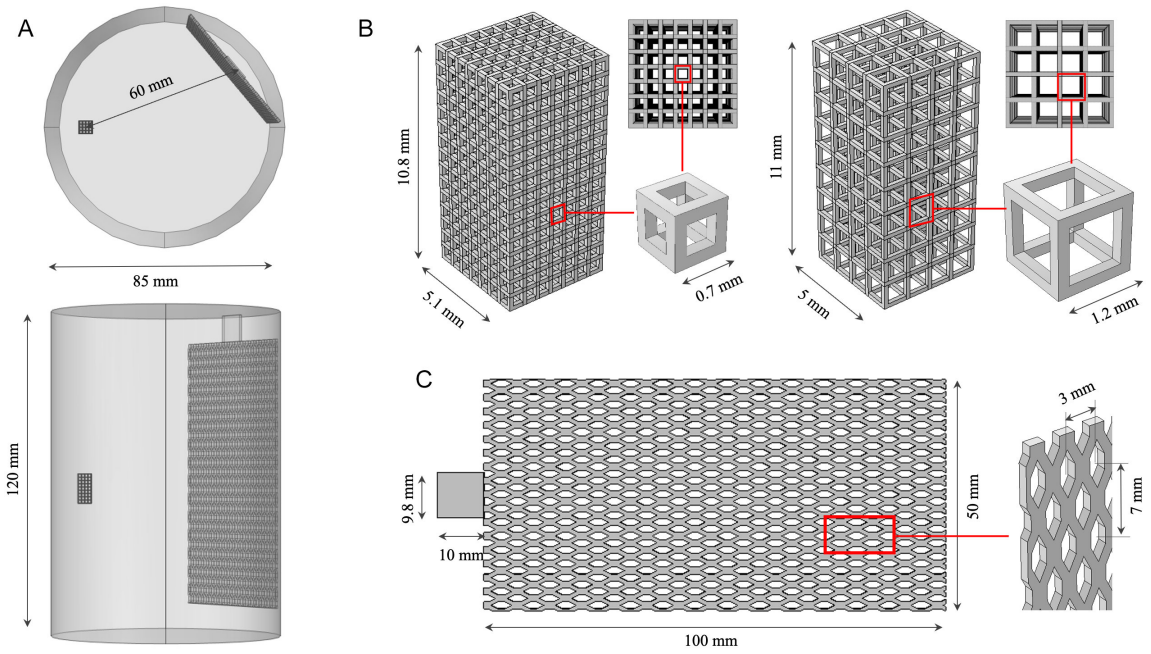


FIGURE 7 | Numerical model geometry and dimensions. (A) Overall geometry of the electrochemical cell and relative positions of the cathode and anode. (B) The small-opening (left) and large-opening (right) lattice scaffolds used as cathodes, including the corresponding unit-cell geometries. (C) Diamond-mesh anode with dimensions of the representative mesh element.

to reduce the computational cost while maintaining adequate numerical resolution.

4.7 | Initial and Boundary Conditions

The initial and boundary conditions were defined to reproduce the electrical conditions of the experimental setup. Initially, the electric potential was set to 0 V throughout the computational domain. Three applied DC voltage differences between the anode and cathode, corresponding to 2, 3, and 4 V, were considered as the electrical boundary conditions. For each simulation case, the electric potentials of the two electrodes were prescribed to achieve the corresponding voltage difference, while the remaining external boundaries of the electrolyte domain were treated as electrically insulating.

4.8 | Domain Conditions

The computational domain comprised three material regions: the electrolyte (seawater), the cathodic lattice-scaffold (316L stainless-steel), and the anode mesh (platinized titanium). Electrical conductivity was assigned to each domain according to its corresponding material properties and used to define the local relationship between the electric field and current density. For the liquid domain, the electrical conductivity of seawater was set to 50 mS/cm, representative of seawater at approximately 25 °C [45]. The cathode and anode domains were assigned electrical conductivities on the order of 10^6 S/m, consistent with values reported for 316L stainless-steel and titanium, respectively [46–49]. These values are several orders of magnitude greater than the conductivity of the electrolyte. Consequently, the potential drop within the solid electrodes is negligible compared with that across the electrolyte, such that the electric potential distribution within the simulation cell is governed primarily by the electrolyte conductivity, electrode geometry, and applied electrical boundary conditions.

4.9 | Characterization of Electrically Mineralized Structural Composites

The mineral gain, M_m, was determined gravimetrically as

$$M_m = m_{\text{after}} - m_{\text{before}} \tag{4}$$

where m_{before} is the dry mass of the 316L stainless-steel lattice scaffold before electrodeposition and m_{after} is the dry mass measured after electrodeposition. Thus, M_m represents the net dry mass increase rather than a direct volumetric filling fraction. No explicit corrosion correction was applied; however, the 0 V immersion-only control (Figure S1) showed negligible dry-mass change after 168 h, indicating that passive immersion effects, residual salt accumulation, and corrosion-related mass changes were limited under the conditions used here. To account for differences in the total electrical charge delivered among the experimental conditions, M_m was additionally normalized by the cumulative charge passed at the corresponding treatment time, M_m/Q, and reported in units of mg/C (Figure S3C,D).

Optical microscopy was performed using an Axio Imager microscope equipped with an AxioCam ERc5s digital camera and controlled using the ZEN 2 Blue software (ZEISS, Oberkochen, Germany) to examine mineral growth within individual lattice units. Whole-scaffold imaging was conducted using a stereomicroscope (SMZ-171, Motic, British Columbia, Canada) to assess the macroscopic mineral deposition.

SEM imaging was performed in secondary electron mode using an FEI Quanta 650 (Thermo Fisher Scientific, Waltham, MA), and

15272648, 0, Downloaded from https://advanced.onlinelibrary.wiley.com/doi/10.1002/adem.71325 by Guido Musso - Politecnico Di Torino Sist. Bibl Del Polit Di Torino , Wiley Online Library on [14/10/2026]. See the Terms and Conditions (https://onlinelibrary.wiley.com/terms-and-conditions) on Wiley Online Library for rules of use; OA articles are governed by the applicable Creative Commons License

elemental distributions were obtained by area-scan EDS analysis with an Oxford AZtec system (Oxford Instruments, Abingdon, UK). Air-dried specimens were mounted on SEM stubs using double-sided carbon tape and coated with a 20 nm Au layer using a Desk IV sputter coater (Denton Vacuum, Moorestown, NJ). SEM imaging was performed at 25 kV with a working distance of 10 mm.

The crystalline phase composition of the electrodeposited minerals was determined using XRD. Prior to analysis, the electrodeposited mineral products were mechanically collected from the specimens and ground into fine powders. XRD analyses were performed using a Rigaku Ultima IV diffractometer (Rigaku Holdings Corporation, Japan) with Cu Kα radiation. Diffraction patterns were recorded over a 2θ range of 5°–80°. The obtained patterns were analyzed using Profex software with BGMN Rietveld refinement to identify the crystalline phases and estimate their relative weight fractions. The reported phase fractions should be interpreted semiquantitatively because sampling heterogeneity, preferred orientation, and possible poorly crystalline or amorphous components may affect the absolute values.

Unconfined compression tests were performed on the untreated reference and mineralized specimens using a mechanical tester (LoadTrac III; GeoComp, Acton, MA, USA). The samples were mounted on a gypsum cap to minimize the stress concentration and loaded at a strain rate of 1%/min. Compressive stress, σ, was calculated by dividing the measured axial load by the nominal cross-sectional area of the pristine scaffold (Table 1) so that untreated and mineralized specimens could be compared based on the original lattice geometry. Axial strain, ε, was calculated by normalizing the axial displacement by the initial height of the pristine scaffold. The apparent compressive modulus, E_{app}, was calculated as the stress at a reference strain of 1% divided by the corresponding strain (0.01) after seating correction. For the small-opening lattice, which did not exhibit a distinct peak stress within the tested strain range (Figure 5), the stress at 8% strain, $\sigma_{8\%}$, was used as its characteristic stress metric. For the large-opening lattice, the peak stress, σ_{peak}, was defined as the maximum stress measured during compression, and the residual stress, σ_{res}, was calculated as the average stress over the postbuckling region between 7.5% and 8% strain. Three specimens ($N = 3$) were tested for each combination of lattice geometry and treatment condition, with the mechanical metrics summarized in Table S1.

Acknowledgments

Yeong-Man Kwon acknowledges the support of the National Research Foundation of Korea (NRF) grant funded by the Korean government (MSIT) (RS-2025-00553627).

Funding

This study was supported by the National Research Foundation of Korea (Grant RS-2025-00553627).

Conflicts of Interest

The authors declare no conflicts of interest.

Data Availability Statement

All the data supporting the findings of this study are available from the corresponding author upon request.

References

1. J. Taheri-Shakib and A. Al-Mayah, "Dynamics of Localized Accelerated Corrosion in Reinforced Concrete: Voids, Corrosion Products, and Crack Formation," *Ceramics International* 50, no. 22 (2024): 48755–48767, https://doi.org/10.1016/j.ceramint.2024.09.229.

2. Y. Yuan, X. Jiang, and X. Liu, "Predictive Maintenance of Shield Tunnels," *Tunnelling and Underground Space Technology* 38 (2013): 69–86, https://doi.org/10.1016/j.tust.2013.05.004.

3. U. M. Angst, "Challenges and Opportunities in Corrosion of Steel in Concrete," *Materials and Structures* 51, no. 1 (2018): 4, https://doi.org/10.1617/s11527-017-1131-6.

4. H. Pan and X. Yin, "Research on Durability of Underground Lining Structures Using Damage Theory," *Scientific Reports* 15, no. 1 (2025): 18957, https://doi.org/10.1038/s41598-025-03451-4.

5. K. P. V. Robles, N. Gucunski, and S.-H. Kee, "Evaluation of Steel Corrosion-Induced Concrete Damage Using Electrical Resistivity Measurements," *Construction and Building Materials* 411 (2024): 134512, https://doi.org/10.1016/j.conbuildmat.2023.134512.

6. L. Maragoni, P. A. Carraro, and M. Quaresimin, "Effect of Voids on the Crack Formation in a [45/−45/0]s Laminate Under Cyclic Axial Tension," *CompTest* 91 (2015): 493–500, https://doi.org/10.1016/j.compositesa.2016.02.018.

7. M. Velu and S. Bhat, "Experimental Investigations of Fracture and Fatigue Crack Growth of Copper–Steel Joints Arc Welded Using Nickel-Base Filler," *Materials & Design* 67 (2015): 244–260, https://doi.org/10.1016/j.matdes.2014.11.026.

8. S. R. Abid, G. Murali, R. A. Al-Ameri, A. A. Abbass, and S. H. Ali, "Experimental Evaluation and Reliability Analysis of Void Configuration Effect on the Compressive Strength of Self-Compacting Concrete Exposed to Elevated Temperatures," *Case Studies in Construction Materials* 23 (2025): e05246, https://doi.org/10.1016/j.cscm.2025.e05246.

9. A. Sayam, A. N. M. M. Rahman, M. S. Rahman, et al., "A Review on Carbon Fiber-Reinforced Hierarchical Composites: Mechanical Performance, Manufacturing Process, Structural Applications and Allied Challenges," *Carbon Letters* 32, no. 5 (2022): 1173–1205, https://doi.org/10.1007/s42823-022-00358-2.

10. P. Nuaklong, P. Jongvivatsakul, V. Phanupornprapong, et al., "Self-Repairing of Shrinkage Crack in Mortar Containing Microencapsulated Bacterial Spores," *Journal of Materials Research and Technology* 23 (2023): 3441–3454, https://doi.org/10.1016/j.jmrt.2023.02.010.

11. A. F. Rotta Loria, D. Shirole, G. Volpatti, A. Guerini, and D. Zampini, "Engineering Concrete Properties and Behavior Through Electrodeposition: A Review," *Journal of Applied Electrochemistry* 53, no. 2 (2023): 193–215, https://doi.org/10.1007/s10800-022-01770-2.

12. G. M. Luz and J. F. Mano, "Mineralized Structures in Nature: Examples and Inspirations for the Design of New Composite Materials and Biomaterials," *ICCM-17: Composites in Biomedical Applications* 70, no. 13 (2010): 1777–1788, https://doi.org/10.1016/j.compscitech.2010.05.013.

13. E. Luso and P. B. Lourenço, "Experimental Characterization of Commercial Lime Based Grouts for Stone Masonry Consolidation," *Construction and Building Materials* 102 (2016): 216–225, https://doi.org/10.1016/j.conbuildmat.2015.10.096.

14. S. Joshi, S. Goyal, A. Mukherjee, and M. S. Reddy, "Microbial Healing of Cracks in Concrete: A Review," *Journal of Industrial Microbiology and Biotechnology* 44, no. 11 (2017): 1511–1525, https://doi.org/10.1007/s10295-017-1978-0.

15272648, 0, Downloaded from https://advanced.onlinelibrary.wiley.com/doi/10.1002/adem.71325 by Guido Musso - Politecnico Di Torino Sist. Bibl Del Polit Di Torino , Wiley Online Library on [14/10/2026]. See the Terms and Conditions (https://onlinelibrary.wiley.com/terms-and-conditions) on Wiley Online Library for rules of use; OA articles are governed by the applicable Creative Commons License

15. W. Li, B. Dong, Z. Yang, et al., "Recent Advances in Intrinsic Self-Healing Cementitious Materials," *Advanced Materials* 30, no. 17 (2018): 1705679, https://doi.org/10.1002/adma.201705679.

16. A. Xin, Y. Su, S. Feng, et al., "Growing Living Composites With Ordered Microstructures and Exceptional Mechanical Properties," *Advanced Materials* 33, no. 13 (2021): 2006946, https://doi.org/10.1002/adma.202006946.

17. N. Wang, Y. Deng, S. Liu, and L. Chen, "Study on the Performance of New Cement-Based Underwater Building Crack Repair Materials Based on Response Surface Analysis," *Scientific Reports* 15, no. 1 (2025): 18499, https://doi.org/10.1038/s41598-025-01137-5.

18. S. da Rocha Gomes, L. Ferrara, L. Sánchez, and M. S. Moreno, "A Comprehensive Review of Cementitious Grouts: Composition, Properties, Requirements and Advanced Performance," *Construction and Building Materials* 375 (2023): 130991, https://doi.org/10.1016/j.conbuildmat.2023.130991.

19. C. Carré, A. Zanibellato, M. Jeannin, R. Sabot, P. Gunkel-Grillon, and A. Serres, "Electrochemical Calcareous Deposition in Seawater. A Review," *Environmental Chemistry Letters* 18, no. 4 (2020): 1193–1208, https://doi.org/10.1007/s10311-020-01002-z.

20. C. Carré, A. Zanibellato, N. Achgare, et al., "Electrochemical Limestone Synthesis in Seawater Binds Metal Grids and Sediments for Coastal Protection," *Environmental Chemistry Letters* 18, no. 5 (2020): 1685–1692, https://doi.org/10.1007/s10311-020-01019-4.

21. L. Zadi, P. Turcry, A. Soive, et al., "Physico-Chemical Stability Evaluation of a Sedimentary Agglomerates Use for the Coastal Protection," *Journal of Coastal Conservation* 27, no. 2 (2023): 12, https://doi.org/10.1007/s11852-023-00940-4.

22. A. Landivar Macias, S. D. Jacobsen, and A. F. Rotta Loria, "Electrodeposition of Calcareous Cement From Seawater in Marine Silica Sands," *Communications Earth & Environment* 5, no. 1 (2024): 442, https://doi.org/10.1038/s43247-024-01604-3.

23. Y.-M. Kwon, and A. F. Rotta Loria, "Electrochemical Cementation of Granular Materials With Different Fabric," *Applied Materials Today* 38 (2024): 102235, https://doi.org/10.1016/j.apmt.2024.102235.

24. I. Nishimura and H. Matsubara, "Electrodeposition-Based Self-Healing Technique for Structures With Loosely Compacted Sand," *Soils and Foundations* 64, no. 6 (2024): 101535, https://doi.org/10.1016/j.sandf.2024.101535.

25. L. Zadi, A. Soive, P. Turcry, et al., "Evolution Mechanisms of an Artificial Calco-Magnesian Agglomerate in Seawater: Analysis of Powder by Experiments and Numerical Modeling," *Coasts* 5, no. 4 (2025): 37, https://doi.org/10.3390/coasts5040037.

26. K.-C. Lai, C. Tsai, S.-Y. Yen, K.-K. Tseng, J.-W. Yeh, and P.-Y. Chen, "Fabrication of Novel 316L Stainless Steel Scaffolds by Combining Freeze-Casting and 3D-Printed Gyroid Templating Techniques," *Materials Science and Engineering: A* 915 (2024): 147200, https://doi.org/10.1016/j.msea.2024.147200.

27. W. M. Haynes, D. R. Lide, and T. J. Bruno, "CRC Handbook of Chemistry and Physics: A Ready-Reference Book of Chemical and Physical Data," in 2016th–2017th, 97th ed. (CRC Press, 2016).

28. D. Mei, Z. D. He, Y. L. Zheng, D. C. Jiang, and Y.-X. Chen, "Mechanistic and Kinetic Implications on the ORR on a Au(100) Electrode: pH, Temperature and H–D Kinetic Isotope Effects," *Physical Chemistry Chemical Physics* 16, no. 27 (2014): 13762–13773, https://doi.org/10.1039/C4CP00257A.

29. M. Chatenet, B. G. Pollet, D. R. Dekel, et al., "Water Electrolysis: From Textbook Knowledge to the Latest Scientific Strategies and Industrial Developments," *Chemical Society Reviews* 51, no. 11 (2022): 4583–4762, https://doi.org/10.1039/D0CS01079K.

30. S. Dresp, F. Dionigi, M. Klingenhof, and P. Strasser, "Direct Electrolytic Splitting of Seawater: Opportunities and Challenges," *ACS Energy Letters* 4, no. 4 (2019): 933–942, https://doi.org/10.1021/acsenergylett.9b00220.

31. C. Barchiche, C. Deslouis, D. Festy, et al., "Characterization of Calcareous Deposits in Artificial Seawater by Impedance Techniques: 3—Deposit of $CaCO_3$ in the Presence of Mg(II)," *Electrochimica Acta* 48, no. 12 (2003): 1645–1654, https://doi.org/10.1016/S0013-4686(03)00075-6.

32. American Society for Testing and Materials, "ASTM D1141-98 Standard for Standard Practice for the Preparation of Substitute Ocean Water," (n.d.).

33. J. Zachara, S. Brantley, J. Chorover, et al., "Internal Domains of Natural Porous Media Revealed: Critical Locations for Transport, Storage, and Chemical Reaction," *Environmental Science & Technology* 50, no. 6 (2016): 2811–2829, https://doi.org/10.1021/acs.est.5b05015.

34. M. Nooraiepour, M. Masoudi, and H. Hellevang, "Probabilistic Nucleation Governs Time, Amount, and Location of Mineral Precipitation and Geometry Evolution in the Porous Medium," *Scientific Reports* 11, no. 1 (2021): 16397, https://doi.org/10.1038/s41598-021-95237-7.

35. A. Neville and A. P. Morizot, "Calcareous Scales Formed by Cathodic Protection—An Assessment of Characteristics and Kinetics," *Journal of Crystal Growth* 243, no. 3-4 (2002): 490–502, https://doi.org/10.1016/S0022-0248(02)01532-4.

36. N. Devi, A. Wagner, J. Lopez, A. Guerini, D. Zampini, and A. F. Rotta Loria, "Mechanistic Insights Into Electrodeposition in Seawater at Variable Electrochemical Potentials," *Advanced Sustainable Systems* 8, no. 4 (2024): 2300446, https://doi.org/10.1002/adsu.202300446.

37. Q.-N. Wang, Y. Qiao, W. Qin, et al., "Bubble Dynamics During Hydrogen Evolution Reaction Over Fluidizable Electrocatalyst Particles," *Industrial & Engineering Chemistry Research* 64, no. 9 (2025): 5087–5098, https://doi.org/10.1021/acs.iecr.4c04934.

38. J. R. Lake, Á. M. Soto, and K. K. Varanasi, "Impact of Bubbles on Electrochemically Active Surface Area of Microtextured Gas-Evolving Electrodes," *Langmuir* 38, no. 10 (2022): 3276–3283, https://doi.org/10.1021/acs.langmuir.2c00035.

39. L. J. Gibson, "Cellular Solids," *MRS Bulletin* 28, no. 4 (2003): 270–274, https://doi.org/10.1557/mrs2003.79.

40. V. S. Deshpande, N. A. Fleck, and M. F. Ashby, "Effective Properties of the Octet-Truss Lattice Material," *Journal of the Mechanics and Physics of Solids* 49, no. 8 (2001): 1747–1769, https://doi.org/10.1016/S0022-5096(01)00010-2.

41. G. Falzone, G. P. Falla, Z. Wei, et al., "The Influences of Soft and Stiff Inclusions on the Mechanical Properties of Cementitious Composites," *Cement and Concrete Composites* 71 (2016): 153–165, https://doi.org/10.1016/j.cemconcomp.2016.05.008.

42. F. Fernandes, S. Manari, M. Aguayo, et al., "On the Feasibility of Using Phase Change Materials (PCMs) to Mitigate Thermal Cracking in Cementitious Materials," *Cement and Concrete Composites* 51 (2014): 14–26, https://doi.org/10.1016/j.cemconcomp.2014.03.003.

43. N. Solomon and I. Solomon, "Effect of Deformation-Induced Phase Transformation on AISI 316 Stainless Steel Corrosion Resistance," *Engineering Failure Analysis* 79 (2017): 865–875, https://doi.org/10.1016/j.engfailanal.2017.05.031.

44. J. M. Bastidas, J. L. Polo, C. L. Torres, and E. Cano, "A Study on the Stability of AISI 316L Stainless Steel Pitting Corrosion Through Its Transfer Function," *Corrosion Science* 43, no. 2 (2001): 269–281, https://doi.org/10.1016/S0010-938X(00)00082-2.

45. A. Revil, L. M. Cathles III, S. Losh, and J. A. Nunn, "Electrical Conductivity in Shaly Sands With Geophysical Applications," *Journal of Geophysical Research: Solid Earth* 103, no. B10 (1998): 23925–23936, https://doi.org/10.1029/98JB02125.

46. P. Huang, Y. Ding, J. Li, L. Xu, and Y. Xie, "Conductivity Estimation of Non-Magnetic Materials Using Eddy Current Method," *Nondestructive Testing and Evaluation* 38, no. 1 (2023): 130–146, https://doi.org/10.1080/10589759.2022.2077939.

15272648, 0, Downloaded from https://advanced.onlinelibrary.wiley.com/doi/10.1002/adem.71325 by Guido Musso - Politecnico Di Torino Sist. Bibl Del Polit Di Torino , Wiley Online Library on [14/10/2026]. See the Terms and Conditions (https://onlinelibrary.wiley.com/terms-and-conditions) on Wiley Online Library for rules of use; OA articles are governed by the applicable Creative Commons License

47. K. A. Ibrahim, B. Wu, and N. P. Brandon, "Electrical Conductivity and Porosity in Stainless Steel 316L Scaffolds for Electrochemical Devices Fabricated Using Selective Laser Sintering," *Materials & Design* 106 (2016): 51–59, https://doi.org/10.1016/j.matdes.2016.05.096.

48. R. W. Powell and R. P. Tye, "The Thermal and Electrical Conductivity of Titanium and Its Alloys," *Journal of the Less Common Metals* 3, no. 3 (1961): 226–233, https://doi.org/10.1016/0022-5088(61)90064-9.

49. E. Villabona, B. E. Moussaoui, F. Veiga, A. Suárez, E. Aldalur, and P. Rivero, "Microstructure and Corrosion Performance of WAAM-HW 316 L Stainless Steel and ER70S-6 In-Situ Alloyed Bimetallic Walls," *Scientific Reports* 16, no. 1 (2026): 22629, https://doi.org/10.1038/s41598-026-53665-3.

Supporting Information

Additional supporting information can be found online in the Supporting Information section.

15272648, 0, Downloaded from https://advanced.onlinelibrary.wiley.com/doi/10.1002/adem.71325 by Guido Musso - Politecnico Di Torino Sist. Bibl Del Polit Di Torino , Wiley Online Library on [14/10/2026]. See the Terms and Conditions (https://onlinelibrary.wiley.com/terms-and-conditions) on Wiley Online Library for rules of use; OA articles are governed by the applicable Creative Commons License